Generating Fano Resonances in a Single-Waveguide Silicon Nanobeam Cavity for Efficient Electro-Optical Modulation

Jianhao Zhang, Xavier Le Roux, Elena Durán-Valdeiglesias, Carlos Alonso-Ramos, Delphine Marris-Morini, Laurent Vivien, Sailing He, Eric Cassan

Generating Fano Resonances in a Single-Waveguide Silicon Nanobeam Cavity for Efficient Electro-Optical Modulation

Jianhao Zhang,[†,§] Xavier Leroux,[†] Elena Durán-Valdeiglesias,[†] Carlos Alonso-Ramos,[†] Delphine Marris-Morini,[†] Laurent Vivien,[†] Sailing He,[*,§] and Eric Cassan[*,†]

[†]Centre for Nanoscience and Nanotechnology (C2N), CNRS, University Paris-Sud, University Paris-Saclay, 91120 Palaiseau Cedex, France

[§]Centre for Optical and Electromagnetic Research, Zijingang Campus, Zhejiang University, Hangzhou 310058, China

ABSTRACT: A method for generating Fano resonance in a standalone silicon nanobeam cavity is reported and investigated thoroughly. The proposed approach eliminates the inconvenience from the unexpected side-coupled bus waveguide of previous Fano cavity geometries and unlocks new opportunities to develop ultracompact and ultrafast silicon electro-optical modulators. Taking advantage from a spatial-division multiplexing principle of operation between transverse electric modes, a sharp resonant mode and an efficient flat background mode are simultaneously generated in the same silicon channel for the realization of efficient Fano resonances. Unambiguous asymmetric spectral line shapes are experimentally demonstrated in the near-infrared around λ = 1.55 μm correlated to analytical and numerical methods. The best identified mode for optical modulation presents an extinction ratio of 23 dB for a $\Delta\lambda$ = 366 pm wavelength detuning, while its Q factor is limited to only 5600. For the same wavelength detuning, this extinction ratio is ∼14 dB higher than that of the classical Lorentzian cavity exhibiting the same Q factor. Electro-optical modulation based on the silicon Fano cavity and exploiting the plasma dispersion effect is proposed and quantitatively studied, showing energy consumption as low as few fJ/bit. The overall gathered results show that the proposed Fano cavity scheme addressed in this paper presents an interesting potential for low-power-consumption silicon electro-optical modulation and provides new insight into the advantages and applications of Fano resonances in nanophotonics.

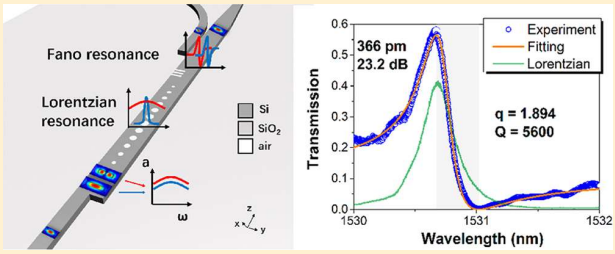

KEYWORDS: *Fano photonic crystal cavity, asymmetric line shape, spatial-division multiplexing, subwavelength optics, mode mixing, electro-optical modulation*

The rapidly increasing demand for optical interconnects leads to the strong requirement of ultralow power consumption and tens-to-hundreds-gigabit devices, among which silicon optical modulators play an essential role. Microresonators including micro rings/disks and photonic crystal cavities, which feature a small footprint and relatively small driven signal for high extinction ratio[1] (e.g., up to 15 dB), have been found to be a promising solution to enable on-chip silicon modulators[2−7] and compact integrated photonic switches.[8−10] However, to ease the burden from the considerable photon lifetime in an ultra-high-quality-factor (Q) cavities, which would be detrimental to the target modulated bandwidth, resonators designed for high-bit-rate modulators usually have limited Q factors of a few thousands. This sacrifice of Q factors results in a larger power consumption of tens to hundreds of femtojoules per bit[5,11,12] for acceptable extinction ratios (>∼8 dB). Approaches like different-signal driving[13] and vertical P−N structures[14] for silicon disk resonators have been implemented to reduce power consumption. However, these kinds of doping schemes are complex and challenging with respect to fabrication accuracy control. Therefore, new and simple solutions are expected for low-power-consumption and high-bit-rate optical modulation.

In this context, Fano resonances, which arise from the interference of a discrete resonant mode and a continuum background,[15] present an efficient ON/OFF transition in a more reduced wavelength detuning between maximum reflection and maximum transmission than the classical Lorentzian-type cavities of similar quality factors. This specific behavior can be used to address the bandwidth-power trade-off of silicon resonant optical modulators and potentially minimize the power consumption of silicon switching and modulation devices. Different types of Fano-resonance-based cavities have already been proposed including spatial membrane structures,[16] plasmonic resonators,[17] and integrated side-coupled one/two-dimensional (1D/2D) photonic crystal cavities.[18−21] Thanks to the advances in fabrication technology, novel integrated devices based on these Fano cavities such as nonreciprocal transmission structures,[22] Fano lasers,[23] and switches[24] have been demonstrated. Especially, an all-optical high-bit-rate modulation behavior combining the free carrier response of indium

phosphide and a Fano cavity was demonstrated.[24,25] Among earlier demonstrated integrated Fano cavities, most previous structures consist of a bus waveguide and a side-coupled photonic crystal cavity.[18−21] When implemented with photonic wires, e.g., within a nanobeam cavity scheme, the first drawback of such configurations arises from the high sensitivity of the bus waveguide/cavity region optical coupling ratio on the technological fabrication imperfections of the structure (in particular on the width of the bus waveguide).[26] The second stems from the fact that the cross-sectional structure of the modulator is intrinsically both asymmetric and more extensive than a simple waveguide one, which complicates the realization of the doping profiles of the PN junction and increases both the capacitance of the whole structure and the access resistances to the polarization electrodes. The obstacle to the realization of fast active cavities based on PN junctions is not related to the realization of the junction itself. The flexible use of PN junctions[27] was indeed demonstrated in 2D photonic crystal active cavities, but this excellent work did not exploit the specifically steep spectral signature of Fano optical cavities, leaving a field of investigation for further progress in terms of power consumption and modulation speed. For the full exploitation of the Fano signature of active cavities, it is particularly important to look for fully integrable configurations in a single waveguide (strip or strongly engraved rib). In this direction, Fano resonance was observed in a single nanobeam cavity,[28] but Fano generation mode mixing between interfering channels was only made at the collection fiber level stage, degradation of Fano generation was observed with the fiber location, and a design methodology for a flexible and systematic Fano generation process still remains unsolved.

Targeting these issues, we address here the investigation of the combination of nanoresonators and control electrodes to develop a new class of Fano resonance silicon modulators aiming at a dramatic reduction in power consumption without sacrificing bandwidth. Design, fabrication, and characterization of sharp and effective Fano resonances in a simple standalone waveguide structure for optical switching and modulation are reported. The mechanism adopted for realizing an effective Fano resonance in a single waveguide geometry without any side-coupled bus waveguide[17−25] is initially introduced, followed by the systematic investigation of the behavior and robustness of Fano spectra by both theoretical and experimental characterizations. Our analysis, stemming from analytical and quantitative analysis, gives new insight into the advantages of Fano resonances for optical modulation schemes and indicates room for further optimization. Although sacrificing the capability for extending to more bus/cavity channels, our cavity effectively compresses the physical dimensions of a Fano cavity and provides room to design PN junctions nearly as easily as in a single-wire waveguide. Combining with rib nanobeam structures[27,29] or nanoarm-assisted nanobeam resonators,[30] the reported new Fano cavity scheme can be expanded for developing low-power-consumption optical modulators based on the plasma dispersion effect.

PRINCIPLE

As is well known, a Fano resonance arises from the interference between a discrete resonance and a continuum[22] and can be practically implemented in a planar photonic platform by placing a side-coupled bus waveguide (the "continuum") in the vicinity of a photonic cavity (the "discrete resonance"), whose coupling and decay rates are controlled by a small partially transmitting element (PTE), as illustrated in Figure 1(a). Compared to this

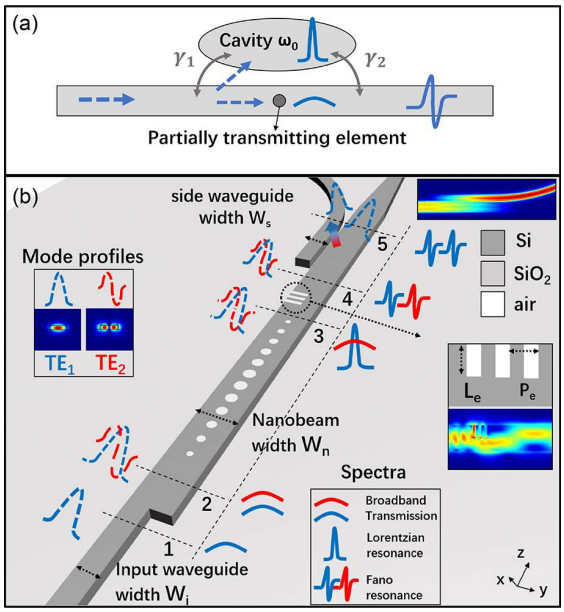

Figure 1. (a) Schematic of a classical integrated Fano cavity. γ_1 and γ_2 are the decay rates due to cavity modes−waveguide modes coupling. (b) Schematic of the proposed standalone Fano cavity, consisting of an MMI-like input structure, a nanobeam cavity, a subwavelength mixer, and a directional coupler. The blue and red dashed curves represent the spatial mode profiles (bottom right inset) of the TE_1 and TE_2 propagating modes, respectively. The blue and red solid curves represent the spectral line shapes of the TE_1 and TE2 propagating modes, respectively. Top right inset: The propagating distribution of the TE_2 propagating mode coupled with and converted into the TE_1 mode of the side waveguide. Middle right inset: Zoom-in view of the three-slit subwavelength mixer and the propagating distribution corresponding to a TE_1 mode injection.

classical configuration in which the resonant and transmitting modes are generated in different physical channels and manipulated by the PTE, the method we propose here is to take advantage of a two-mode spatial multiplexing scheme to generate the resonant and the transmitting modes in the same physical optical waveguide, as shown in Figure 1(b). This standalone Fano cavity consists of a single-mode input waveguide, a nanobeam cavity whose cross section supports two transverse electric field (TE) propagating modes (position 2), and a subwavelength mode mixer. The TE_1 and TE_2 propagating modes, which are schematically depicted by the blue/red dashed curves in the bottom left inset of Figure 1(b), have symmetric/asymmetric fields within the waveguide cross-section, respectively. The multimode interference (MMI)-like operation allows a tight control of the balance between the excited TE_1 and TE_2 propagating modes at position 2 through the choice of the narrow (input) and wide (nanobeam) waveguides' widths, labeled w_i and w_n, respectively (see Figure 1(b)). The key to the design is also to widen the contrast between the effective indices of these two modes so that the TE_1 propagating mode strongly feels the influence of the cavity, thus generating a marked spectral resonance, while the second propagating mode, TE_2, is only slightly sensitive to the periodic corrugation of the waveguide geometry and thus presents a very flat transmission spectrum (i.e., an ultrawide resonance). The spectrum of both TE propagating modes are schematically represented by the solid curves in Figure 1(b) at position 3. The nanobeam cavity is followed by a subwavelength mixer for intermixing between the

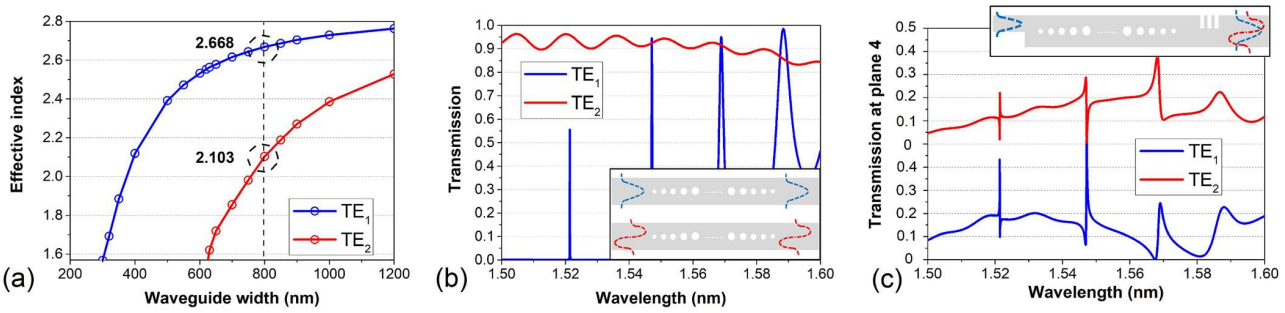

Figure 2. (a) Dispersion curves of the TE modes at 1550 nm wavelength in a 220 nm thick silicon on insulator strip waveguide with different width values (w_n) (plane 2 in Figure 1(b)). (b) Transmission spectra (from plane 2 to plane 3 in Figure 1(b)) of the TE_1 and TE_2 propagating modes through a classical nanobeam cavity with w_n = 800 nm, 50 holes, and 300 nm period. (c) Transmission spectra of the TE_1 and TE_2 propagating modes through the proposed Fano cavity with a 400 nm wide input waveguide. The period, filling factor, and length of the subwavelength hole array are P_e = 200 nm, ff = 0.5, and L_e = 400 nm, respectively. Other parameters are identical to that reported in (b). In each figure, the TE_1 and TE_2 propagating modes are depicted by blue and red solid curved lines or circles, respectively. Structures corresponding to the (b) and (c) configurations are shown in the insets, in which the TE_1 and TE_2 spatial mode profiles are displayed by blue and red dashed lines, respectively.

TE_1 propagating mode narrow resonance and the TE_2 mode wide resonance, respectively, which produces two Fano resonances, i.e., for each of the TE modes. An additional narrow side waveguide forms a directional coupler to convert the TE_2 propagating mode to the TE_1 mode of the side waveguide (see the left inset of Figure 1(b)). Five planes marked by black dashed lines (1,2, 3, 4, and 5) at different positions in Figure 1(b) are used to illustrate the structure principle of operation: plane 1 at the input waveguide, plane 2 before the cavity, plane 3 before the mode mixer, plane 4 after the mode mixer, and plane 5 at the bifurcation of the output directional coupler.

In order to study the feasibility of the proposed single-waveguide principle of operation, eigenmode solving and FDTD methods were extensively used to calculate the mode dispersion and field and power transmission levels of the TE modes in the nanobeam structure. The corresponding platform we considered starts from a typical silicon-on-insulator (SOI) photonic platform with a 220 nm thick silicon core and a 2 μm thick buried silicon dioxide layer. The dispersion curves of both TE propagating modes (at plane 2) obtained for different nanobeam widths (w_n) are presented in Figure 2(a). In principle, in order to provide a high transmission level for the TE_2 mode with a weak perturbation from the nanobeam cavity, the difference in effective index values between the TE_1 and TE_2 propagating modes should be as large as possible to prevent Bragg reflection for the TE_2 mode. A waveguide width w_n = 630 nm ($n_{eff,TE1} \approx 2.55$ and $n_{eff,TE2} \approx 1.6$) corresponds to the ideal value, but due to the rapid change of the TE_2 propagating mode dispersion close to this condition, this option can lead to fabrication-sensitivity issues. Thus, a moderate value w_n = 800 nm was selected (throughout this work), providing an acceptable index contrast between the TE_1 and TE_2 propagating modes of ~0.565.

Next, a nanobeam cavity with a 50-hole array under a period of 300 nm was considered. To obtain a resonant high quality (Q) factor and a high transmission for the TE_1 mode, the hole radii were tapered from 100 nm in the center to 70 nm in a 15-period length.[31] Extra 10-hole mirror sections with identical 70 nm radius holes were added at the end of each taper. The total length of the nanobeam cavity was close to 15 μm. The calculated transmission spectra (from plane 2 to plane 3 in Figure 1(b)) for both TE propagating modes are shown in Figure 2(b). The simulated quality factor/transmission values with TE_1 input (merely TE_1 propagating mode in the nanobeam waveguide) for the first and second cavity modes are 230 000/55% and 19 000/95%, respectively. For the TE_2 propagating mode, an average transmission larger than 90% is obtained in the 1500 to 1600 nm wavelength range. Although the peak transmissions of these two TE propagating modes are not exactly balanced, the related excitation ratio can easily be engineered by adjusting the input waveguide width of the MMI-like structure to find the right balance between the two optical modes.

To mix both TE propagating modes after the nanobeam cavity (plane 4 in Figure 1(b)), a subwavelength mixer consisting of a few asymmetrically located rectangle-shape etch holes (Figure 1(b)) is placed after the resonator. The period, filling factor, and length of the mixer region hole are P_e = 200 nm, ff = 0.5, and L_e = 400 nm, respectively. Both TE propagating modes in the nanobeam waveguide excite the first two order modes of the subwavelength structure, which are converted back into the TE propagating mode again after the mixer. By carefully selecting the mixer length, we achieve a TE_1–TE_1 and TE_2–TE_1 mixing efficiency of ~45% and ~35%, respectively. These coupling efficiencies are obtained here from a 3-N (3 hole) subwavelength mixer (optimizing methodology for the subwavelength mixer is presented in the Supporting Information). The simulated propagating distribution corresponding to a TE_1 light injection is shown in the middle right inset in Figure 1(b). The mode interference behavior after the subwavelength mixer is an obvious signature of multimode generation. The transmission levels of the TE propagating modes through the complete device (inset in Figure 2(c), i.e., from plane 1 to plane 4) including the input waveguide width w_i = 400 nm (which provides excitation efficiencies of 55% and 40% for TE_1 and TE_2 modes, respectively), the MMI-like structure, the nanobeam cavity, and the subwavelength mixer, are reported in Figure 2(c).

Unambiguous Fano line spectra for the TE_1 propagating mode (blue curve in Figure 2(c)) and the TE_2 mode (red curve in Figure 2(c)) are observed, which confirms the adequate interference of the resonant and the flat spectra. Interestingly and as anticipated, the TE_2 mode (red curve in Figure 2(c)) also exhibits a Fano spectrum line shape, since part of the TE_1 and TE_2 modes are indeed coupled back to the TE_2 mode as well after the mixer. Incomplete destructive interferences marked by the appreciable but not complete Fano dips (transmission does not drop to 0) result from the unbalanced TE_1/TE_2 energy levels. Each of both Fano resonance behaviors can be separately optimized by adjusting either the TE_1–TE_1, TE_2–TE_1 mixing efficiencies or the TE_2–TE_2, TE_1–TE_2 ones.

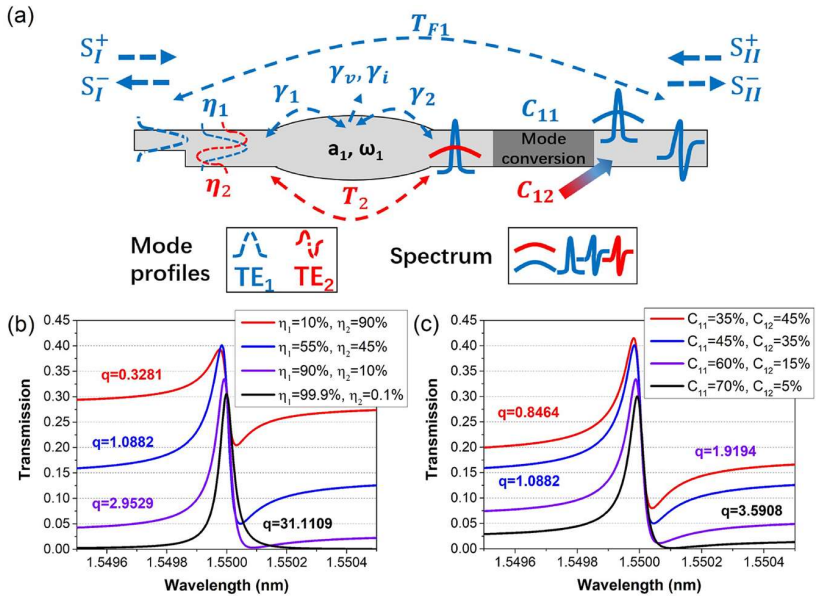

Figure 3. (a) Schematic of the dynamics of optical waves in a standalone two-port waveguide nanobeam Fano cavity. TE_1 and TE_2 propagating modes are marked by blue and red dashed curves, respectively. The spectrum of TE_1 and TE_2 propagating modes are depicted by the blue and red curves, respectively. (b, c) Transmission of the TE_1 mode versus the varying excitation efficiencies η_1, η_2 and mixing efficiencies C_{11}, C_{12}. The exchange efficiencies in (b) are fixed as $C_{11} = 0.45$, $C_{12} = 0.35$, while the excitation efficiencies in (c) are $\eta_1 = 0.55$, $\eta_2 = 0.45$, respectively. Both (b) and (c) share the following parameters: $\omega_1 = 2\pi$*193.414 THz, $T_2 = 90\%$, $Q_1 = \frac{\omega_1}{2\gamma_1} = 7 \times 10^4$, $Q_v = \frac{\omega_1}{2\gamma_v} = 1.6 \times 10^5$, and $Q = \frac{\omega_1}{2\gamma_t} \approx 30\,000$.

ANALYTICAL DESCRIPTION OF FANO RESONANCE

To further study the generation of Fano resonances in such a standalone cavity structure, we performed complementarily analytical calculation using the temporal coupled-mode theory[18,32] (TCMT). The equivalent schematic view of the cavity dynamics is shown in Figure 3(a). The total structure can be considered as a two-port scattering system. S_I^+ and S_I^- are the forward and backward field amplitudes from port I (left side port), respectively. S_{II}^+ and S_{II}^- share the same definitions for port II (right side port). t_{F1} is the complex transmission coefficient of the electric field (then $T_{F1} = |t_{F1}|^2$ is the power transmission) of the TE_1 propagating mode after the mixer (energy of TE_1 mode in plane 4 normalized to that at plane 1). For a nanobeam cavity with a resonant angular frequency ω_1 and corresponding electric field a_1 for the TE_1 mode, the decay rate for this resonant mode due to coupling to the two feeding waveguides and the decay rate due to out-of-plane scattering and intrinsic absorption are γ_1, γ_2, γ_v, and γ_i, respectively. Therefore, the total decay rate (TE_1 propagating mode) can be written as $\gamma_t = \gamma_1 + \gamma_2 + \gamma_v + \gamma_i$. The energy excitation efficiency from the TE_1 propagating mode to the TE_1 and TE_2 modes in the MMI-like structure (defined in Figure 2(b)) are labeled by η_1 and η_2, respectively. Meanwhile the efficiencies from the TE_1 and TE_2 modes to the TE_1 mode of the subwavelength mixer at the output port are labeled as C_{11} and C_{12}, respectvely. The transmission of the nanobeam cavity for the TE_2 propagating mode called T_2 ($T_2 = |t_2|^2$) can be assumed as nearly uniform due to the weak interaction of this mode with the array of patterned holes.

According to the TCMT and considering a detuning of angular frequency $\delta_r = \omega - \omega_1$, the coupled equations of the resonant and backward waves can be written as follows:

$$\frac{da(t)}{dt} = (-i\delta_r - \gamma_t)a + \sqrt{2\gamma_1}e^{i\theta_1}\sqrt{\eta_1}S_I^+ \tag{1}$$

$$S_I^- = r_m\sqrt{\eta_1}S_I^+ + \sqrt{2\gamma_1}e^{i\theta_1}a \tag{2}$$

$$S_{II}^- = \sqrt{2\gamma_2}e^{i\theta_2}a\sqrt{C_{11}} + \sqrt{\eta_2}S_I^+t_2\sqrt{C_{12}}ie^{i\Delta\theta} \tag{3}$$

in which θ_1 and θ_2 are the phase factors of the cavity waveguide modes at the left and right ports, respectively. $\Delta\theta$ is the phase difference between the TE_1 and TE_2 propagating modes, which is counted from the MMI-like interface to the front plane of the mixer. The reflection coefficient of the nanobeam cavity mirrors for the TE_1 mode is r_m, which can be considered as 1 for simplification (confirmed by an estimated reflection power level at a slightly off-resonant wavelength, which indicated a reflection coefficient of ~0.98).

For steady-state condition, $da(t)/dt = 0$ and the field transmission coefficient for the TE_1 mode through the whole structure ($T_{F1} = |t_{F1}|^2$) can be written as

$$t_{F1} = \frac{S_{II}^-}{S_I^+} = \frac{2\sqrt{\gamma_1\gamma_2\eta_1C_{11}}e^{i(\theta_1+\theta_2)}}{i\delta_r + \gamma_t} + i\sqrt{\eta_2C_{12}}t_2e^{i\Delta\theta} \tag{4}$$

For symmetric cavity design, $\theta_1 = \theta_2$, $\gamma_1 = \gamma_2$, and for a highly confined cavity mode, $e^{i(\theta_1+\theta_2)} = \cos(\theta_1 + \theta_2) + i\sin(\theta_1 + \theta_2) = -r_m \approx -1$;[23] therefore

$$t_{F1} = \frac{S_{II}^-}{S_I^+} \approx \frac{-2\gamma_1\sqrt{\eta_1C_{11}}}{i\delta_r + \gamma_t} + i\sqrt{\eta_2C_{21}}t_2e^{i\Delta\theta} \tag{5}$$

If there is no excitation of the TE_2 mode and no mixer region after the cavity ($\eta_1 = C_{11} = 1$, $\eta_2 = C_{12} = 0$), then

$$T_F = |t_t|^2 \approx \frac{4\gamma_1^2}{\delta_r^2 + \gamma_t^2} \tag{6}$$

The total transmission of the TE_1 propagating mode then goes back to a typical Lorentzian shape.

For a case where $\eta_2 \neq 0$, $C_{21} \neq 0$:

$$T_{F1} \approx = \frac{\frac{4\gamma_1^2}{\gamma_t^2}\eta_1 C_{11}}{\frac{\delta_r^2}{\gamma_t^2}+1} + \eta_2 t_2^2 C_{12} + \frac{\frac{4\gamma_1}{\gamma_t}t_2\sqrt{\eta_1 C_{11}\eta_2 C_{12}}}{\frac{\delta_r^2}{\gamma_t^2}+1}\left(\frac{\delta_r}{\gamma_t}\cos\Delta\theta + \sin\Delta\theta\right) \quad (7)$$

Assuming that the phase relative variable is written as $C_p = -\frac{\delta_r}{\gamma_t} + \frac{\delta_r}{\gamma_t}\cos\Delta\theta + \sin\Delta\theta$, we simplify T_{F1} as

$$T_{F1} \approx \eta_2 T_2 C_{12}\frac{\left(\frac{\delta_r}{\gamma_t} + \frac{2\gamma_1\sqrt{\eta_1 C_{11}}}{\gamma_t t_2\sqrt{\eta_2 C_{12}}}\right)^2}{\frac{\delta_r^2}{\gamma_t^2}+1} + \eta_2 T_2 C_{12}\frac{\left(1 + \frac{4\gamma_1\sqrt{\eta_1 C_{11}}}{\gamma_t t_2\sqrt{\eta_2 C_{12}}}C_p\right)}{\frac{\delta_r^2}{\gamma_t^2}+1} \quad (8)$$

Assuming that $\frac{\delta_r}{\gamma_t} = \epsilon$, $\frac{2\gamma_1\sqrt{\eta_1 C_{11}}}{\gamma_t t_2\sqrt{\eta_2 C_{12}}} = q$, and taking into account that the total energy of the TE_2 propagating mode coupled back to the TE_1 mode is $T_{12} = \eta_2 T_2 C_{12}$, we can simplify eq 8 as

$$T_{F1} \approx T_{12}\frac{(\epsilon+q)^2}{\epsilon^2+1} + T_{12}\frac{(1+2qC_p)}{\epsilon^2+1} \quad (9)$$

The first term of eq 9 is the same as the traditional expression for Fano resonance in a two-port cavity.[33] The variable q is the asymmetric parameter, which quantifies the Fano spectrum asymmetry. The normalized energy amplitude of the continuum part of the TE_1 propagating mode, e.g., the T_{21}, becomes the amplitude coefficient of the Fano spectrum in eq 2. Similarly in the classical Fano spectrum, the amplitude coefficient is the transmission of the partially transmitting element.[15] However, the above equations indicate that the phase quantity also contributes to the transmission and can cause a small deviation to the perfect Fano line shape. By controlling C_p, this phase-related item can be minimized and high-quality Fano line shapes can then be obtained. As a whole, the above analytical calculation shows that the obtained pseudo-Fano expression opens room to design a sharp Fano-like behavior. Analysis of the TE_2 mode can be made similarly and is not shown here.

To study the effect of excitation efficiencies and mixing efficiencies on the spectrum, we assume that $\Delta\theta = 0$ (then $C_p = \epsilon(-1 + \cos\Delta\theta) + \sin\Delta\theta = 0$) for simplification; thus

$$T_t = T_{12}\frac{(\epsilon+q)^2}{\epsilon^2+1} + T_{12}\frac{1}{\epsilon^2+1} \quad (10)$$

On the basis of eq 10, we accordingly adjust the energy ratio of the TE_1/TE_2 propagating modes and the mixing efficiencies to search the optimization operation point. The related details are shown in Figure 3(b) and (c). In these plots, clear Fano curves presenting sharp spectral transitions and high extinction ratio are demonstrated from $\eta_1 = 0.1$ and $\eta_1 = 0.9$. The best configuration for Fano behavior, indicated by $q \approx 1$ (the largest asymmetry), is generally linked to the most rapid change (maximum slope) of the structure spectral transmission. This condition is satisfied here when $\eta_1 = 0.55$, as shown in Figure 3(b). Especially, the comparison between the $\eta_1 = 0.9$ and $\eta_1 = 0.999$ cases shows that values of η_1 close to 1 are necessary to recover a Lorentzian shape cavity spectral line shape.

We also investigated the effect of the mixer with different coupling efficiencies (C_{11} and C_{12}) on the Fano spectra, as shown in Figure 3(c). The q parameter variation is much more limited than in the previous case, and the spectra keep a fairly marked Fano shape even in the severe $C_{11};C_{12}$ = 70%;5% condition, which indicates the robustness of the proposed Fano cavity scheme against variations of the mixer geometry. Overall, the main trends reported in Figure 3(b) and (c) provide a design strategy to target a trade-off between correct Fano line shapes and large extinction ratio values.

EXPERIMENTS

The scanning electron microscopy (SEM) picture of a typical fabricated device is shown in Figure 4(a). The gap (Figure 1(b)) between the nanobeam waveguide and the side waveguide (w_s = 400 nm) is 150 nm here. A straight coupling length of 16 μm was chosen to completely couple the TE_2 propagating mode in the nanobeam waveguide to the TE_1 mode in the side waveguide. Then the side waveguide was turned into a bend waveguide with a radius of 40 μm for an ultralow loss separation of both modes. The performances of this directional coupler were confirmed by 3D-FDTD simulations and from many fabricated devices' characterizations. The mixer dimensions consisted of three rectangle etched holes with a 200 nm period and a 50% filling factor, each rectangle hole having a length (L_e in Figure 1(b)) of half w_n, i.e., of 200 nm. The width of the input waveguide was chosen as 500 nm since the experimental transmission of the resonant mode was usually lower than the theoretical one. Other parameters of the nanobeam cavity were directly inherited from the design stages, i.e., a nanobeam waveguide width w_n = 800 nm, N = 50 (number of holes), and a hole radius profile quadratically tapered from 100 nm in the center to 70 nm at the edges.

The transmission curves of the full structure are shown in Figure 4(b). Clear Fano line shapes for the first- and second-order cavity modes are observed, with resonance wavelengths located at around 1515 and 1531 nm, respectively, which are close to the values (1510 and 1533 nm) obtained from the 3D-FDTD simulation in Figure 2(b). Simulated distributions for these two modes are presented in the insets of Figure 4(b). Simultaneous Fano line shapes of the second cavity mode in the nanobeam and side waveguides are also shown in Figure 4(c), as the blue and orange curves, respectively. Zoomed-in views of the transmission curves around the two spectral resonances are shown in Figure 4(d) and (e), respectively. The blue circles and the orange solid curves are experimental results and fitting curves from eq 9, respectively.

In Figure 4(d), we see that in a wavelength detuning of 56 pm the cavity optical transmission experiences a transition drop of about 17 dB. To experimentally obtain the quality factor, another device with same parameters but an input width of 700 nm was further analyzed. This wide-input device can be considered as a classical nanobeam cavity without any TE_2 propagating-mode excitation (Figure 2(b)). According to our previous analysis, the transmission spectrum is then fairly close to a Lorentzian resonance. Using $Q = \frac{\Delta\omega}{\omega_0}$, a Q factor of ~32 000 was obtained (the transmission of this Lorentzian spectrum is low and not shown in Figure 4(d)). The Q factor value was also extracted from eq 9, by fitting the experimental Fano spectrum. The asymmetric total decay rate γ_t was 2π*2.96 GHz, which indicated a Q factor of 34 000, well coincident with that given by the Lorentzian-type device. The asymmetric parameter q was estimated as q = 1.6335, i.e., close to the perfect Fano condition

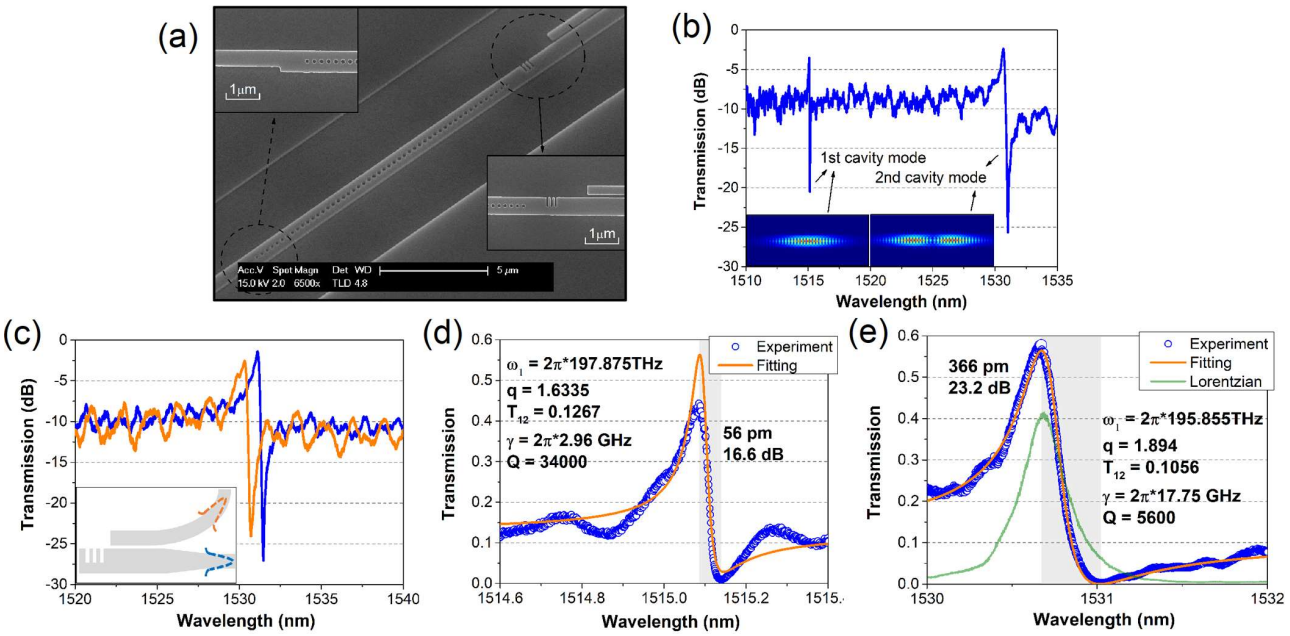

Figure 4. (a) SEM views of fabricated devices. The MMI-like structure and subwavelength mixer are shown in the top-left and bottom-right insets, respectively. (b) Experimental transmission of the nanobeam waveguide. (c) Experimental transmission around the second cavity mode detected in nanobeam and side waveguides, depicted by blue and orange curves, respectively. (d) Experimental transmission and fitting curve of the first cavity mode of the nanobeam waveguide, depicted by blue circles and an orange curve, respectively. (e) Experimental transmission and fitting curve of the second cavity mode of the nanobeam waveguide, depicted by blue circles and orange curves, respectively. The Lorentzian curve is labeled by a green curve, while transitions between maximum and minimum are depicted by gray regions.

(i.e., $|q| \approx 1$), proving the consistency of the carried-out optimization. In addition, the total measured energy transmission from the TE_2 propagating mode to the TE_1 one ($T_{12} = \eta_2 T_2 C_{12}$) was found to be around 0.1267. Considering the excitation ratio of the TE_2 mode (η_2) for a 500 nm width input waveguide of about 0.3 and the nanobeam transmission (T_2) of 0.9 and a mixing efficiency (c_{21}) of 0.35, this value of T_{21} (0.1267) is thus in good agreement with analytical prediction (0.0945).

Similar analysis for the second cavity mode was performed as well, from which a more than 23.2 dB extinction ratio was obtained for a wavelength detuning of 366 pm, as shown in Figure 4(e). The calculated asymmetric parameter q, the Q factor, and the total transmission T_{12}were 1.894, 5600, and 0.1056, respectively (the phase variables C_p for both cases were calculated to be close to zero and are not shown). Using a device made of an identical nanobeam cavity but with a 700 nm width input waveguide, an overall transmission of $T = 0.88$ was experimentally monitored. According to the estimation[31] $T = \left(\frac{Q_{total}}{Q_{wg}}\right)^2$ and the classical relationship $\frac{1}{Q_{total}} = \frac{1}{Q_{wg}} + \frac{1}{Q_{i+v}}$, quality factors Q_{wg} and Q_{i+V}, both accounting for waveguide coupling and intrinsic absorption and vertical losses, were estimated as $Q_{wg} = 5930$ and $Q_{i+V} = 100\,000$, respectively. This estimate thus demonstrated the negligible nature of optical losses by absorption and out-of-plane scattering. An experimental Lorentzian spectrum with nearly the same Q factor of 5600 is reported as well (green curve) in Figure 4(e) for comparison, which is clearly less efficient. For a lossless Lorentzian resonance $\frac{\gamma_t^2}{(\omega_0 - \omega)^2 + \gamma_t^2}$ with the same Q factor of 5600 ($\gamma_t = 2\pi$*17.75 GHz), the extinction ratio (ER) for a wavelength detuning of 366 pm ($\Delta\omega \approx 2\pi$*46.83 GHz) is $-10\log\left(\frac{\gamma_t^2}{(\Delta\omega)^2 + \gamma_t^2}\right) = 9$ dB. This value is 14 dB smaller than that of the experimentally reported Fano resonance (~23 dB). From another perspective, with the same Q factor (5600) and ER (23 dB), the wavelength detuning required in a Lorentzian case is 1.96 nm ($\Delta\omega \approx 2\pi$*251 GHz), which would lead to a much higher driven power. Increasing Q is obviously an option to ease the burden from ER-frequency detuning trade-off. For example, a Q as high as 40 000 in the Lorentzian-spectrum cavity is capable of providing the same efficiency; however such a high Q would lead to an excessive photon lifetime, raising an obstacle to the bandwidth of electro-optical modulators based on this structure.[11] For example, for a quality factor of only 10 000, the bandwidth f_{3dB} limited by photon lifetime in already no more than 20 GHz, according to $\frac{1}{f_{3dB}^2} = (2\pi\tau)^2 + (2\pi RC)^2$and $\tau = \frac{\lambda Q}{2\pi c}$. These comparisons indicate the excellent potential of the proposed single-waveguide Fano cavities ($Q \approx 5600$) for ultrafast, efficient electro-optical modulation and switching.

In order to have a clear observation on how Fano resonance is influenced by the balance between modes, a series of configurations with different TE_1/TE_2 excitation ratios were performed by varying the input waveguide width w_i. As shown in Figure 5(a), with the nanobeam width w_n being fixed at 800 nm (again, throughout this work), the out(plane 5)/in(plane 1) excitation efficiency of the TE_1 propagating mode increases with the waveguide width, while the excitation efficiency of the TE_2 mode first reaches a maximum at w_i = 400 nm and then gradually decreases with increasing w_i values. These monotonic trends of the TE_1 mode curve can be understood with the related increased effective index value, which minimizes the impedance mismatch between the input access waveguide and the nanobeam

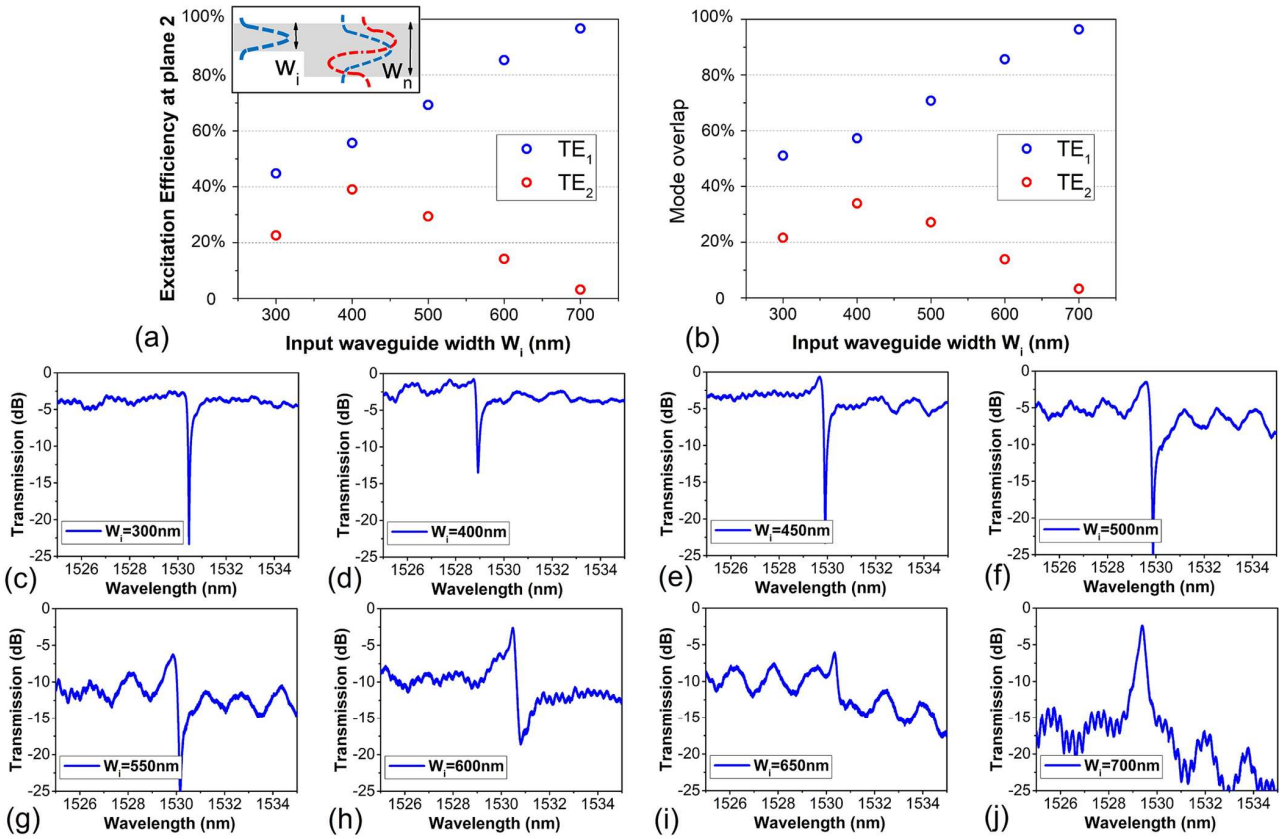

Figure 5. (a) Excitation efficiencies of the TE_1 and TE_2 propagating modes at plane 2 in a nanobeam waveguide with w_n = 800 nm, connected with an input waveguide with different widths w_i ranging from 300 to 700 nm. (b) Corresponding mode overlap between the input waveguide and nanobeam waveguide. (c)−(j) Evolution of the Fano spectrum by varying the width of the input waveguide w_i from 300 to 700 nm, respectively.

waveguide modes. On the other hand, the increased TE_2-mode efficiency arises from an improved effective index matching and the largest mode overlap (Figure 5(b)) at the input/nanobeam waveguide interface. Figure 5(a) indicates that the excitation efficiency of the TE_1/TE_2 mode can be adjusted in a large range (from nearly 55%/40% to infinity). For input waveguide widths larger than 400 nm, the summation of the TE_1 and TE_2 excitation efficiencies (i.e., the summation of blue and red curves in Figure 5(a)) is close to 1, which also indicates an available width range for low-loss light injection. The spectrum evolution of an array of fabricated Fano cavities with different w_i ranging from 300 to 700 nm is reported in Figure 5(c)−(j). The spectrum line shapes first behave as all-pass filters and become asymmetric with increasing input waveguide widths and achieve almost a maximum asymmetry within the range of 500−600 nm of input waveguide width, then coming back to an add-drop-type Lorentzian shape resonator at $w_i \approx 700$ nm. Clear Fano line shapes are widely observed from w_i = 450 nm to 650 nm. This easiness highlights the robustness of our design even in the case of possible tens of nanometers of fabrication errors.

DISCUSSION

Remembering that the limited quality factor (for high bit rate modulation) in a Lorentzian active cavity puts a practical ceiling to the extinction ratio and tends to increase the needed operating voltage swings (usually up to few volts[2]), the most important merit of Fano resonance resonators is to improve the extinction ratio and power consumption by providing a sharp transition between reflection and transmission states. Since our design is intrinsically suitable for PN modulator and switching integrated schemes, one significant further work is here to estimate the power consumption of electro-optic modulators *r* relying on the plasma dispersion effect and the proposed stand-alone Fano resonator.

The proposed PN Fano modulator is shown in Figure 6, and the analysis is performed on the 220 nm SOI platform with 170 rib thickness and 50 nm slab thickness. The Fano cavity is slightly doped in both the side and a depletion region formed in the center. Meanwhile, the free carrier induced index change in silicon can be described at 1.55 μm wavelength by[34]

$$\begin{aligned}\Delta n &= \Delta n_e + \Delta n_h \\ &= -[8.8 \times 10^{-22} \times \Delta N_e + 8.5 \times 10^{-18} \times (\Delta N_h)^{0.8}\end{aligned} \tag{11}$$

Δn_e, Δn_h, ΔN_e, and ΔN_h are here the electron-induced index change, hole-induced index change, the density changes of electrons, and density changes of holes. For a common doping change level of $\Delta N_e = \Delta N_h = 5 \times 10^{17}$, the index change is $\Delta n = -1.7 \times 10^{-3}$. We consider a nanobeam cavity with symmetric PN junctions, i.e., with identical widths for the P-type and N-type regions. The optical index in the P-doped/depletion regions can be considered as 3.4783 and ~3.48, respectively. Since the depletion width of the PN junction can be described as[35]

$$W_d = \left[\frac{2\varepsilon_0\varepsilon_r(N_D + N_A)}{q(N_D\Delta N_A)}\left(V_P + V_{ext} - \frac{2k_BT}{q}\right)\right]^{1/2} \tag{12}$$

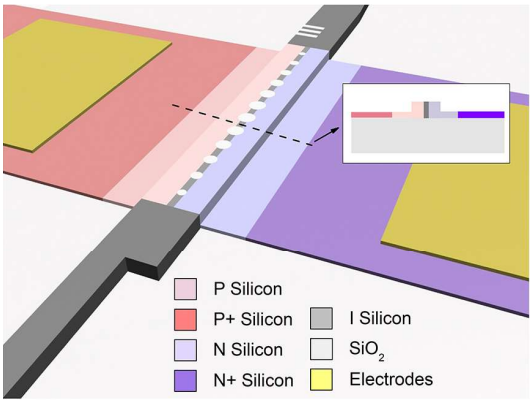

Figure 6. Proposed Fano modulator based on rib silicon PN depletion structure. Inset is the cross-section of the rib structure at the position labeled by the dotted line.

$\varepsilon_0 = 8.8542 \times 10^{-12}$ F/m and $\varepsilon_r = 12$. V_P, V_{ext}, and q are the vacuum silicon dielectric constant, the silicon dielectric constant, the built-in potential, external applied voltage, and the unit charge. k_B is the Boltzmann constant, and T is the temperature fixed at 300 K.

For a 0.35 nm shift of the Fano resonance (consistent with the second cavity mode discussed above, with $Q \approx 5600$ and an extinction ratio larger than 20 dB), the required width change of the depletion region (ΔW_d) calculated by using 3D-FDTD simulation was estimated to about 15 nm. The peak−peak voltage for such a width change at a bias of $V_B \approx -0.5$ V is $\Delta V_{ext} \approx 0.5$ V (i.e., V_{ext} is within the range of $V_B - \Delta V_{ext}/2$ to $V_B + \Delta V_{ext}/2$). Considering an average depletion width of 100 nm and a cavity length $L = 15$ μm, the capacitance of the PN junction is[35]

$$C_d = \varepsilon_0 \varepsilon_r \frac{H_{rib}(\sim 220\ \text{nm})}{W_d} L \approx 4\ \text{fF} \tag{13}$$

Therefore, the energy consumption per bit can be estimated as[11]

$$E = \frac{CV_{PP}^2}{4} = \frac{C_d \Delta V^2}{4} \approx 0.25\ \text{fJ/bit} \tag{14}$$

Even considering a practical capacitance (i.e., an experimental capacitance taking other capacitance and fabrication imperfection into account besides the depletion capacitance) of $C = 50$ fF like for earlier reported ring resonators,[15] the energy consumption per bit is still as low as 3.125 fJ/bit. Such a low energy consumption per bit, which is supported by the small wavelength detuning of 366 pm required to obtain an ER of 23 dB in the proposed Fano cavity with a low Q factor of 5600, is not possible to achieve in Lorentzian-line-shape resonant modulators. For the first cavity mode of $Q \approx 34\,000$ (0.056 nm shift for ER > 15 dB), the energy consumption per bit is reduced down to $E \approx 0.5$ fJ/bit. Besides, asymmetric doping profiles could be further considered to optimize the active structure performances.[36] The absorption resulting from the free carriers[31] we obtained for this structure is $\Delta\alpha = 7.25$ cm^{-1}, from which we derived an imaginary part ($n = n + ik$, at 1550 nm wavelength) of a refractive index of $\Delta k = 0.89 \times 10^{-4}$. Taking this value into account, we recalculated the quality factor of the nanobeam cavity with and without free carriers. The quality factor for the second cavity mode in the passive case is 1.89×10^4, while it was estimated to be 1.29×10^4 when free carriers were accounted for, indicating an additional decay rate of only $\Delta\gamma_i = 2\pi$*2.38 GHz. Comparing this value to the experimental total decay rate of the second mode ($\gamma_t = 2\pi$*17.75 GHz), we observe that the impact of free-carrier absorption on the Fano resonance decay is small. This result brings a confirmation that the cavity quality factor is dominated by the strong coupling[30] between the propagating mode in the feeding waveguide and the cavity mode, rather than by free-carrier absorption losses (i.e., with the notations of the paper, the resonance is mainly governed by γ_1, γ_2, and γ_v, rather than γ_i), let alone the further lossy contribution from fabrication. Thanks to this small additional decay rate, q is only weakly influenced by free carriers so that the asymmetric spectral line shape of the cavity is preserved in the active modulation configuration.

CONCLUSION

In this paper, a clear and marked Fano resonance is achieved in a single-waveguide silicon nanobeam cavity, which provides a novel path to develop monolithically integrated high-frequency and low-power-consumption silicon modulators. By using the mode-diverse response of a single nanobeam cavity, controlling the spatial-division multiplexing and mode mixing in the multimode waveguide section, we realize a sharp resonant mode and a flat background mode in the same silicon channel for flexible generation of Fano resonances. Unambiguous asymmetric spectrum line shapes were experimentally observed, presenting a 23.2 dB extinction ratio within a 366 pm detuning for one of the cavity modes ($Q = 5600$), the factors of merits of which cannot be reached in classical Lorentzian-type integrated active cavities of similar Q factors controlled with the identical wavelength detuning. Our investigation, based on an analytical model supported by a quantitatively numerical calculation, reports a thoughtful strategy for the optimization of the pseudo-Fano resonances. The energy consumption of active modulation in a single-waveguide Fano cavity using the plasma dispersion effect was estimated to be less than a few fJ/bit, giving competitive potential to the realization of low-power-consumption silicon optical modulators operating at high-data bit rates (≫1 Gbits s^{-1}). We believe that the proposed Fano cavity scheme opens room for the realization of single-waveguide silicon modulators going beyond the current state of the art.

METHODS

Fabrication and Characterization. An SOI wafer with a 220 nm silicon thickness was used for fabrication. Device fabrication was based on electron-beam lithography, ICP-RIE etching, and a wet cleaning process.[37] A tunable laser (Yenista TUNICS, T100S) operating in the 1520−1640 nm wavelength range, a polarizer, and a power meter (Yenista CT400) were used for charactering the devices. A couple of grating couplers were used for fiber-chip in and out interfacing. All the transmission curves were normalized to straight waveguides with identical grating couplers.

ASSOCIATED CONTENT

Supporting Information

The Supporting Information is available free of charge on the ACS Publications website at DOI: 10.1021/acsphotonics.8b00867.

Principle, optimization, and robustness of the subwavelength mixer (PDF)

REFERENCES

(1) Sacher, W. D.; Green, W. M. J.; Assefa, S.; Barwicz, T.; Shank, S. M.; Vlasov, Y. A.; Poon, J. K. S. Controlled Coupling in Silicon Microrings for High-Speed, High Extinction Ratio, and Low-Chirp Modulation. *CLEO.* **2011**, PDPA8.

(2) Xu, Q.; Schmidt, B.; Pradhan, S.; Lipson, M. Micrometre-scale silicon electro-optic modulator. *Nature* **2005**, *435*, 325−327.

(3) Manipatruni, S.; Preston, K.; Chen, L.; Lipson, M. Ultra-low voltage, ultra-small mode volume silicon microring modulator. *Opt. Express* **2010**, *18*, 18235−18242.

(4) Dong, P.; Liao, S.; Liang, H.; Qian, W.; Wang, X.; Shafiiha, R.; Feng, D.; Li, G.; Zheng, X.; Krishnamoorthy, A. V.; Asghari, M. High-speed and compact silicon modulator based on a racetrack resonator with a 1 V drive voltage. *Opt. Lett.* **2010**, *5*, 3246−3248.

(5) Tanabe, T.; Nishiguchi, K.; Kuramochi, E.; Notomi, M. Low power and fast electro-optic silicon modulator with lateral p-i-n embedded photonic crystal nanocavity. *Opt. Express* **2009**, *17*, 22513.

(6) Nguyen, H. C.; Hashimoto, S.; Shinkawa, M.; Baba, T. Compact and fast photonic crystal silicon optical modulators. *Opt. Express* **2012**, *20*, 22465−22474.

(7) Terada, Y.; Kondo, K.; Abe, R.; Baba, T. Full C-band Si photonic crystal waveguide modulator. *Opt. Lett.* **2017**, *42*, 5110−5112.

(8) Soref, R.; Hendrickson, J. R.; Sweet, J. Simulation of germanium nanobeam electrooptical 2 × 2 switches and 1 × 1 modulators for the 2 to 5 μm infrared region. *Opt. Express* **2016**, *24*, 9396−9382.

(9) Zhou, H.; Qiu, C.; Jiang, X.; Zhu, Q.; He, Y.; Zhang, Y.; Su, Y.; Soref, R. Compact, submilliwatt, 2 × 2 silicon thermo-optic switch based on photonic crystal nanobeam cavities. *Photonics Res.* **2017**, *5*, 108−112.

(10) Soref, R. Tutorial: Integrated-photonic switching structures. *APL Photonics* **2018**, *3*, 021101.

(11) Dong, P.; Liao, S.; Feng, D.; Liang, H.; Zheng, D.; Shifiiha, R.; Kung, C.-C.; Qian, W.; Li, G.; Zheng, X.; Krishnamoorthy, A. V.; Asghari, M. Low Vpp, ultralow-energy, compact, high-speed silicon electro-optic modulator. *Opt. Express* **2009**, *17*, 22484−22490.

(12) Rosenberg, J.; Green, W. M. J.; Assefa, S.; Gill, D. M.; Barwicz, T.; Yang, M.; Shunk, S. M.; Vlasov, Y. A. A 25 Gbps silicon microring modulator based on an interleaved junction. *Opt. Express* **2012**, *20*, 26411−26423.

(13) Zortman, W. A.; Lentine, A. L.; Trotter, D. C.; Watts, M. R. Low-voltage differentially-signaled modulators. *Opt. Express* **2011**, *19*, 26017−26026.

(14) Timurdogan, E.; Sorace-Agaskar, C. M.; Sun, J.; Hosseini, E. S.; Biberman, A.; Watts, M. R. An ultralow power athermal silicon modulator. *Nat. Commun.* **2014**, *5*, 4008.

(15) Miroshnichenko, A. E.; Flach, S.; Kivshar, Y. S. Fano resonances in nanoscale structures. *Rev. Mod. Phys.* **2010**, *82*, 2257−2298.

(16) Zhou, W.; Zhao, D.; Shuai, Y.-C.; Yang, H.; Chuwongin, S.; Chadha, A.; Seo, J.-H.; Wang, K. X.; Liu, V.; Ma, Z.; Fan, S. Progress in 2D photonic crystal Fano resonance photonics. *Prog. Quantum Electron.* **2014**, *38*, 1−74.

(17) Limonov, M. F.; Rybin, M. V.; Poddubny, A. N.; Kivshar, Y. S. Fano resonance in photonics. *Nat. Photonics* **2017**, *11*, 543−554.

(18) Fan, S. Sharp asymmetric line shapes in side-coupled waveguide-cavity systems,. *Appl. Phys. Lett.* **2002**, *80*, 908−910.

(19) Yu, P.; Hu, T.; Qiu, H.; Ge, F.; Yu, H.; Jiang, X.; Yang, J. Fano resonances in ultracompact waveguide Fabry-Perot resonator side-coupled lossy nanobeam cavities. *Appl. Phys. Lett.* **2013**, *103*, 091104.

(20) Heuck, M.; Kristensen, P. T.; Yuriy, E.; Mørk, J. Improved switching using Fano resonances in photonic crystal structures. *Opt. Lett.* **2013**, *38*, 2466−2468.

(21) Nozaki, K.; Shinya, A.; Matsuo, S.; Sato, T.; Kuramochi, E.; Notomi, M. Ultralow-energy and high-contrast all-optical switch involving Fano resonance based on coupled photonic crystal nanocavities. *Opt. Express* **2013**, *21*, 11888.

(22) Yu, Y.; Chen, Y.; Hu, H.; Xue, W.; Yvind, K.; Mørk, J. Nonreciprocal transmission in a nonlinear photonic-crystal Fano structure with broken symmetry,. *Laser & Photon. Rev.* **2015**, *9*, 241−247.

(23) Yu, Y.; Xue, W.; Semenova, E.; Yvind, K.; Mørk, J. Demonstration of a self-pulsing photonic crystal Fano laser. *Nat. Photonics* **2017**, *11*, 81−84.

(24) Yu, Y.; Heuck, M.; Hu, H.; Xue, W.; Peucheret, C.; Chen, Y.; Oxenløwe, L. K.; Yvind, K.; Mørk, J. Fano resonance control in a photonic crystal structure and its application to ultrafast switching. *Appl. Phys. Lett.* **2014**, *105*, 061117.

(25) Yu, Y.; Hu, H.; Oxenløwe, L. K.; Yvind, K.; Mørk, J. Ultrafast all-optical modulation using a photonic-crystal Fano structure with broken symmetry. *Opt. Lett.* **2015**, *40*, 2357−2360.

(26) Fegadolli, W. S.; Pavarelli, N.; O'Brien, P.; Njoroge, S.; Almeida, V. R.; Scherer, A. Thermally Controllable Silicon Photonic Crystal Nanobeam Cavity without Surface Cladding for Sensing Applications. *ACS Photonics* **2015**, *2*, 470−474.

(27) Shakoor, A.; Nozaki, K.; Kuramochi, E.; Nishiguchi, K.; Shinya, A.; Notomi. Compact 1D-silicon photonic crystal electrooptic modulator operating with ultra-low switching voltage and energy. *Opt. Express* **2014**, *22*, 28623−28634.

(28) Mehta, K. K.; Orcutt, J. S.; Ram, R. J. Fano line shapes in transmission spectra of silicon photonic crystal resonators. *Appl. Phys. Lett.* **2013**, *102*, 081109.

(29) Sodagar, M.; Miri, M.; Eftekhar, A. A.; Adibi, A. Optical bistability in a one-dimensional photonic crystal resonator using a reverse-biased pn junction. *Opt. Express* **2015**, *23*, 2676−2685.

(30) Zhang, J.; He, S. Cladding-free efficiently tunable nanobeam cavity with nanotentacles. *Opt. Express* **2017**, *25*, 12541−12551.

(31) Quan, Q.; Loncar, M. Deterministic design of wavelength scale,ultra-high Q photonic crystal nanobeam cavities. *Opt. Express* **2011**, *19*, 18529−18542.

(32) Suh, W.; Wang, Z.; Fan, S. Temporal Coupled-Mode Theory and the Presence of Non-Orthogonal Modes in Lossless Multimode Cavities. *IEEE J. Quantum Electron.* **2004**, *40*, 1511−1518.

(33) Yoon, J. W.; Magnusson, R. Fano resonance formula for lossy two-port systems,. *Opt. Express* **2013**, *21*, 17751−17759.

(34) Soref, R. A.; Bennett, B. R. Electrooptical Effects in Silicon,. *IEEE J. Quantum Electron.* **1987**, *23*, 123−129.

(35) Zhou, Y.; Zhou, L.; Zhu, H.; Wong, C.; Wen, Y.; Liu, L.; Li, X.; Chen, J. Modeling and optimization of a single-drive push−pull silicon Mach−Zehnder modulator. *Photonics Res.* **2016**, *4*, 153−160.

(36) Marris-Morini, D.; Vivien, L.; Fédéli, J. M.; Cassan, E.; Lyan, P.; Laval, S. Low loss and high-speed silicon optical modulator based on a lateral carrier depletion structure. *Opt. Express* **2008**, *16*, 334−339.

(37) Hoang, T. H. C.; Duran-Valdeuglesias, E.; Alonso-Ramos, C.; Serna, S.; Zhang, W.; Balestrieri, M.; Keita, A.-S.; Caselli, N.; Biccari, F.; Le-Roux, X. R.; Filorama, A.; Gurioli, M.; Vivien, L.; Cassan, E. Narrow-linewidth carbon nanotube emission in silicon hollow-core photonic crystal cavity. *Opt. Lett.* **2017**, *42*, 2228−2231.